Nano Research

Open Access

Research Article

Machine-learning assisted filterless color imaging with donor–acceptor ratio engineered self-driven organic photodetectors

Yujie Xie[1], Xixiang Zhu[1] ✉, Jinpeng Li[1], Haomiao Yu[1], Kai Wang[1], Zhenmei He[1], Yukang Lu[1], Yongchao Xie[1], Henan Li[1], Zheng Chen[1], Hanlin Hu[2], Haizhe Zhong[3], Xiaoxian Zhang[1], Yumeng Shi[1] ✉, and Aiwei Tang[1] ✉

[1] *Key Laboratory of Luminescence and Optical Information, Ministry of Education, School of Physical Science and Engineering, Beijing Jiaotong University, Beijing 100044, China*
[2] *Hoffmann Institute of Advanced Materials, Shenzhen Polytechnic University, Shenzhen 518060, China*
[3] *Shenzhen Key Laboratory of 2D Metamaterials for Information Technology, Institute of Microscale Optoelectronics, Shenzhen University, Shenzhen 518060, China*

Cite this article: *Nano Research*, **2026**, *19*, 94908382. https://doi.org/10.26599/NR.2026.94908382

ABSTRACT: Miniaturized optical wavelength-sensing devices based on solution-processed organic materials hold great promise for integration into portable and wearable technologies. Yet, the realization of self-powered compact wavelength sensors remains elusive. Here, we report a self-powered wavelength sensor built from broadband photodetectors featuring a meticulously engineered PM6:L8-BO active layer. By systematically varying the donor–acceptor stoichiometries and implementing these blends in nano-scale active layers (50 and 100 nm) that modulate the internal optical field distribution, we tailor the spectral responsivity of individual sensor units, yielding distinct wavelength-dependent optoelectronic signatures. An array of these wavelength-discriminating units enables quantitative discrimination and identification of incident light wavelengths. The device accurately resolves wavelengths from 380 to 850 nm with a resolution better than ~ 1 nm, determined through the photocurrent ratio mapping of the four photodetector elements. As a proof of concept, we demonstrate the device's capability in wavelength recognition and full-color imaging, underscoring its potential for compact, self-powered, and versatile optical sensing platforms.

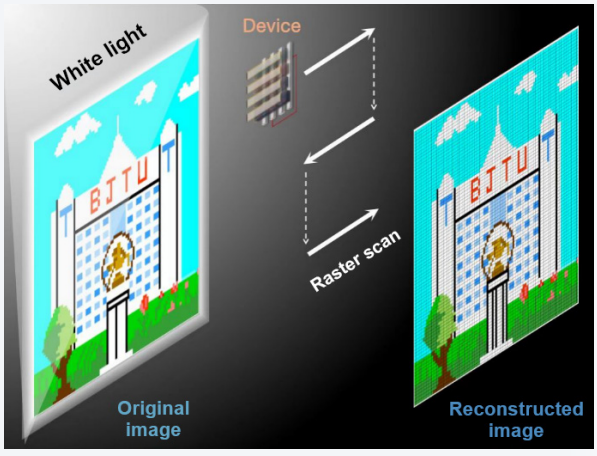

KEYWORDS: self-powered, wavelength sensor, organic photodetectors, distribution of photocurrent ratio, full-color imaging

1 Introduction

Wavelength sensors capable of quantitatively measuring light wavelengths are of paramount importance in applications such as multi-wavelength imaging, spectral analysis, optical communication, environmental monitoring, and medical testing [1–4]. Conventional wavelength sensors are typically realized by integrating broadband inorganic semiconductor photodiodes with dichroic prisms or filter arrays [5–7]. However, these approaches often encounter limitations due to expensive and bulky components with restricted wavelength ranges.

Received: October 4, 2025; **Revised:** December 26, 2025
Accepted: December 29, 2025

✉Address correspondence to Xixiang Zhu, xxzhu@bjtu.edu.cn; Yumeng Shi, ymshi@bjtu.edu.cn; Aiwei Tang, awtang@bjtu.edu.cn

To meet the demand for compact and cost-effective portable wavelength sensors, recent research efforts have been devoted to the miniaturization of photodetectors [8]. As a crucial supplement, filterless sensors have attracted growing attention, with significant progress in developing materials with tunable spectral responses [9, 10]. Among these, arrayed broadband photodetectors combined with computational identification algorithms have successfully replaced bulky spectrometers for wavelength sensing. Representative approaches include modulating the bandgap of nanomaterials [11, 12] and engineering of van der Waals (vdW) heterojunctions with tunable band alignment in two-dimensional materials (2DMs) [13]. For example, bandgap-tunable nanostructured semiconductors, including 0-dimensional (0D) quantum dotS (QDs), one-dimensional (1D) nanowires, and two-dimensional (2D) monolayers, have been fabricated for multispectral imaging or spectral measurement applications. By comparing photocurrents generated under different band

alignment conditions and applying spectral reconstruction algorithms, these sensors can quantitatively distinguish incident light wavelengths [14, 15]. Although filterless wavelength sensors offer advantages for lightweight device scaling, their spectral responses are often sensitive to geometric dimensions [16] or electrically tunable spectral response [17]. Therefore, the performance of these devices is commonly sensitive to the growth condition, layer thickness, interface contacts, and even operating conditions [18].

Additionally, these devices typically have a limited linear dynamic range (LDR) and relatively narrow sensing range [19]. Moreover, external electrical bias is often required for machine learning and spectral reconstruction processes, leading to additional energy consumption [18, 20]. Self-powered devices, by contrast, are well-suited for applications in harsh or remote environments [21]. The built-in electric field in self-powered photodetectors not only reduces energy consumption and enhances sustainability but also facilitates rapid separation of photogenerated carriers, resulting in fast response time. The elimination of external power sources also improves portability, making them ideal for wearable sensors and long-term monitoring. However, an effective strategy for achieving self-powered spectral responses remains underdeveloped.

Solution-processed organic materials offer a low-cost, large-scale fabrication route for optoelectronic devices and image sensors [22]. Photomultiplication effects have been realized in organic semiconducting materials with a high donor–acceptor ratio (typically ~ 100:1) [23]. Recently, tunable spectral responses have also been achieved by controlling photocarrier redistribution via an integrated optical spacer in organic photodetectors (OPDs) under bias [24]. Studies have shown that the performance of organic electronic devices is strongly influenced by the matching of electron donor:acceptor (D:A) ratios [25, 26]. Remarkably, the development of non-fullerene acceptors has shed light on organic electronics, transforming organic photovoltaics into a useful technology [27]. The PM6:L8-BO binary system is a classic D:A combination, enabling organic solar cells with a power conversion efficiency (PCE) exceeding 19% [28, 29].

In this study, we propose a simple yet effective strategy for wavelength-sensitive detection based on chemical composition tuning of the polymer donor PM6 and non-fullerene acceptor L8-BO, achieving a self-driven spectral response. Using tunable photoresponse and reconstruction algorithms, our device functions as a wavelength-sensitive photodetector, distinguishing wavelengths from 380 to 850 nm with a resolution less than 1.2 nm. The solution processability of these organic materials ensures scalable fabrication and uniform device performance. As a proof of concept, we fabricated a 2 × 2 device array for imaging applications, which exhibits high color accuracy. We further demonstrate that a full-color cartoon image can be reproduced using this self-driven wavelength sensor combined with a scanning imaging system. The complementary absorption characteristics of PM6 and L8-BO enable the wavelength-sensitive detection, providing a promising pathway to expand the application of organic optoelectronic devices to wavelength-selective detection and multi-wavelength imaging.

2 Experimental

Materials information: The patterned indium tin oxide (ITO)-coated glass substrates were purchased from Advanced Election Technology Co., Ltd. PM6, L8-BO, and PFN-Br were purchased from Organtec Ltd.

Device fabrication: The ITO glass substrate was ultrasonically cleaned with deionized water, isopropanol, and ethanol for 15 min, then dried with ultrapure nitrogen and treated with ultraviolet (UV) ozone plasma for 1 min. Subsequently, poly(3,4-ethylenedioxythiophene):poly(styrenesulfonate) (PEDOT:PSS) was spin-coated on ITO glass at 5000 rpm and annealed at 150 °C for 15 min. A PM6:L8-BO mixed solution was prepared in chloroform (containing 0.5% 1-chloronaphthalene (CN) additive) and stirred on a magnetic stirrer at 60 °C for 3 h. After cooling to room temperature, the PM6:L8-BO solution was spin-coated onto the PEDOT:PSS layer and annealed at 100 °C for 10 min. The spin-coating process was controlled using a PDMS template to form a 2 mm × 16 mm strip-shaped film. When the PM6:L8-BO ratio was 1:1, two active layers with different thicknesses, 100 (prepared from a 15.4 mg/mL solution) and 50 nm (prepared from a 7.7 mg/mL solution), were fabricated by adjusting the solution concentration while maintaining a fixed spin-coating speed of 3000 rpm. For a PM6:L8-BO ratio of 5:1, a 75 nm thick active layer (7.7 mg/mL) was obtained by spin coating at 1500 rpm. Similarly, for a PM6:L8-BO ratio of 1:5, a 50 nm thick active layer (7.7 mg/mL) was also prepared by spin coating at 2000 rpm. Then the poly(9,9-bis(3'-(N,N-dimethylamino)propyl)fluorene-alt-2,7-(9,9-dioctylfluorene)) dibromide (PFN-Br) was spin-coated on the active layer at 3000 rpm, and then a 100 nm Ag electrode was evaporated in vacuum to form a heterojunction ITO/PEDOT:PSS/photo-active layer/PFN-Br/Ag device. The fabricated wavelength sensor had an active area of 3.8 mm^2.

Device characterization: The incident monochromatic light was obtained by a 150 W xenon lamp coupled with a monochromator. The monochromatic light intensity was measured using a Thorlabs S120VC power meter. The transient photocurrent density of the wavelength sensor was measured using a Keithley 2400 source meter under the modulation by an electronic shutter. All the above measurements were carried out in a high-purity nitrogen-filled glovebox. The absorption spectra of used materials in active layers were obtained by a Shimadzu UV-2600 PC spectrophotometer. The thickness of the optimized wavelength sensor was measured by an AMBIOS technology XP-2 stylus profilometer.

3 Results and discussion

In this work, we developed self-powered photodetector units to discern light of different wavelengths by altering the ratio of donor to acceptor components. Figure 1(a) schematically illustrates the device configuration of the developed wavelength sensor. The cross-sectional scanning electron microscopy (SEM) image in Fig. 1(b) shows the well-defined stratification of the device. The photo-active layer is composed of a PM6:L8-BO blend, where the highest occupied molecular orbital (HOMO) and the lowest unoccupied molecular orbital (LUMO) of PM6 match well with those of the non-fullerene acceptor L8-BO, facilitating efficient exciton dissociation and charge transfer. For the convenience of discussion, we name the donor (PM6) and acceptor (L8-BO) with molar ratios of 1:1, 5:1, and 1:5 as D_1A_1, D_5A_1, and D_1A_5, respectively. In addition, the D_1A_1 with thicknesses of 100 and 50 nm were named D_1A_1-WB and D_1A_1-NB, respectively. As illustrated in Fig. 1(c) and Fig. S2 in the ESM, PM6 and L8-BO exhibit complementary absorption profiles: PM6 predominantly harvested visible photons, whereas L8-BO effectively extended the absorption edge into the near-infrared region. The absorption profile aligns well with the

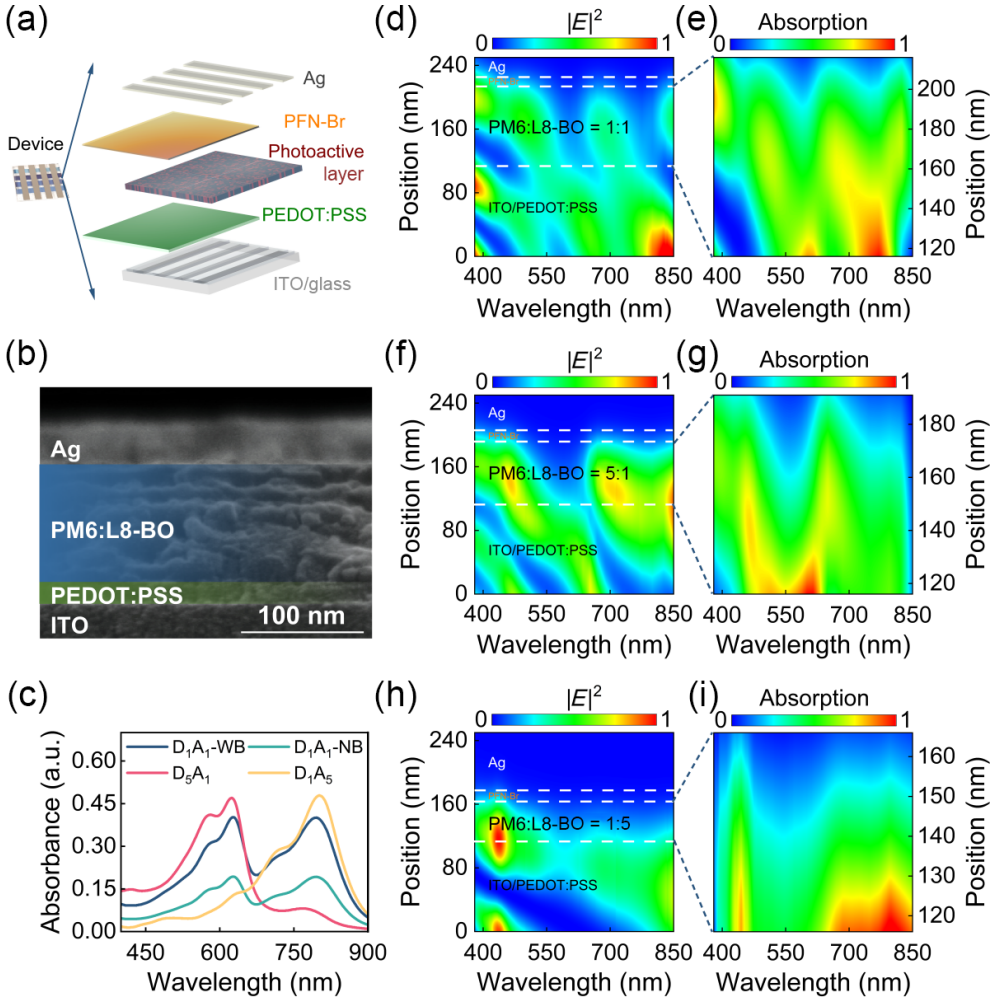

Figure 1 (a) Digital photograph of wavelength sensors (left) and schematic illustration of individual device structure (right). (b) SEM cross-sectional image for a typical device with D_1A_1-WB as photoactive layer. (c) UV–Vis absorption spectra of D_1A_1-WB, D_1A_1-NB, D_5A_1, and D_1A_5. Simulated optical field distribution diagrams for various donor and acceptor ratios of (d) 1:1, (f) 5:1, and (h) 1:5. Corresponding wavelength dependent light absorption capability of devices with D:A ratios of (e) 1:1, (g) 5:1, and (i) 1:5.

solar spectrum, enabling efficient sunlight absorption and providing more photons for photoelectric conversion, thereby enhancing the photocurrent of the devices. Thus, the devices fabricated using a donor/acceptor blend with different chemical ratios of PM6:L8-BO essentially alters the wavelength dependent photocurrent generation.

To achieve the high-resolution, self-powered wavelength discrimination, the photodetector must deliver wavelength-dependent optoelectronic responses. This requirement is fulfilled by tailoring the interaction between the incident light and active layer, which governs the photon absorption, exciton generation, and hence spectral selectivity. A key mathematical basis for the wavelength sensor is the response vector matrix. Indeed, nano-scale structural engineering is fundamental to the wavelength-selective behavior of our OPD array, and the active-layer thickness plays a decisive role in shaping the internal optical field distribution. Our device relies on carefully engineered PM6:L8-BO layers with nanoscale thicknesses of 50 and 100 nm, which were selected based on thickness-dependent optical field simulations. Rigorous optical-field simulations performed across a matrix of D:A ratios and thicknesses were therefore indispensable for identifying conditions that yield strong, wavelength-selective absorption, laying the groundwork for precise wavelength discrimination and high-resolution imaging.

The optical field distributions in the OPDs with the structure of ITO (100 nm)/PEDOT:PSS (15 nm)/PM6:L8-BO (1:1, 5:1, 1:5)/PFN-Br (15 nm)/Ag (100 nm) were simulated using the finite-difference time-domain (FDTD) method [30, 31], as shown in Figs. 1(d) and 1(f). The corresponding refractive indices (n) and extinction coefficients (k) of the blend films are provided in Fig. S3 in the ESM. By simulating optical-field profiles, we reveal how systematically varying the donor:acceptor ratio tailors the light-harvesting efficiency at different wavelengths of light (Figs. 1(g) and 1(i)) and enables the spectral responsive device performance. The underlying principle rests on a direct, quantitative proportionality between the local optical field intensity and the absorbance of material (see the ESM) [32].

$$\langle P_{abs} \rangle = 2\pi\varepsilon_0 c \cdot \frac{nk}{\lambda_0} \cdot |E|^2 \quad (1)$$

where E is the electric field intensity. Across the three stoichiometries, the spatial–spectral interplay between optical field intensity and absorption coefficient suggests the wavelength response of the device.

For the 1:1 ratio, the constructive interference occurs at adjacent depths within the photoactive layer for different wavelengths (Fig. 1(d)). The refractive-index matching of the 1:1 blend to the adjacent transport layers suppresses reflections and establishes a standing-wave resonance that traps light inside the photoactive region, ensuring that the field covers the full absorption band. Combined with the n and k across the visible–near infrared (Vis–NIR) range, the 1:1 ratio yields a broadband absorption profile (Fig. 1(e)) spanning 380–850 nm.

As shown in Fig. 1(f), the 5:1 blend exhibits the wavelength-selective constructive interference. This phenomenon stems from the refractive-index tuning dominated by PM6, where an excess of PM6 elevates the average refractive n of the photoactive layer, leading to a mismatch with the PEDOT:PSS. The modified optical path length was combined with the n and k value characteristics within the Vis–NIR spectral range to form a restricted absorption band (Fig. 1(g)). This absorption band corresponds to the absorption peak of PM6, with a wavelength range of 500–700 nm. This optimization allows for more efficient capture of photons in the specified wavelength range.

Figure 1(h) reveals highly localized constructive interference. Although $|E|^2$ of 1:5 ratio is low-intensity throughout NIR, the blend's extinction coefficient k remains high, yielding the largest $|E|^2 \cdot n \cdot k$ product and the corresponding high optical power of absorbance (Fig. 1(i)).

These results signify that the D:A ratio modulates both the spatial distribution of the electric field and the spectral dependence of absorption, thereby enabling the control over the wavelength response. These simulations indicate that nano-scale cavity interference and field-confinement effects substantially modify the spatial profile of photon absorption and carrier generation, thereby producing the distinct wavelength-dependent responsivities required for accurate wavelength identification.

To investigate the transmission of light at different wavelengths in the active layer, we simulated the optical field distributions at three typical wavelengths (500, 620, and 800 nm) (Fig. S4 in the ESM). Altering the PM6:L8-BO ratio directly reshapes the light energy distribution within the device [33]. During propagation, the $|E|^2$ decays to zero, following Beer–Lambert's law [34, 35].

Figures 2(a) and 2(b) present the photocurrent and external quantum efficiency (EQE) spectra acquired from 380 to 850 nm under monochromatic illumination generated by a xenon arc lamp-monochromator system. The D_1A_1-WB device enables coverage of the entire absorption spectrum. It operates via the photovoltaic effect: The semiconductor PN junction absorbs photons to generate electron–hole pairs, which are separated by the built-in electric field to form electrical signals (Fig. S5 in the ESM). The wavelength dependence of the photocurrent aligns with the absorption characteristics of PM6 (main peak at 620 nm) and L8-BO (main peak at 800 nm), confirming that photogenerated carriers primarily originate from the effective capture and conversion of incident photons by the active layer. Photoresponse measurements of devices with different active layer thicknesses showed that the 100 nm-thick device achieves a maximum photocurrent of 12 μA. However, further increasing the thickness causes a decrease in photocurrent, due to the limited charge diffusion length and inefficient charge collection in thicker films. These findings support the synergistic regulation of photocurrent responses across different wavelength bands using D:A ratios and active layer thickness. This thickness-dependent behavior originates from nano-scale structural engineering, where the 50 and 100 nm active layers impose distinct optical-field distributions critical for wavelength-selective responsivity.

EQE analysis (Fig. 2(b)) showed that the D_1A_1-WB exhibits the highest photon-to-current conversion efficiency across all characterized wavelengths, corresponding to the absorption region. The fabricated OPDs also show excellent linear responses over an illumination intensity range of 0–1000 mW/cm^2 (Fig. 2(c)). In the visible light region, D_1A_1-WB achieves a Wavelength-dependent responsivity (R) up to 0.58 A/W and a detectivity (D) of 4.2×10^{12} Jones (Fig. 2(d)). The R and D of other devices are presented in Figs. S6 and S7 in the ESM. The temporal photocurrent response of the D_1A_1-WB under light with a wavelength of 532 nm is shown in Fig. 2(e), and other devices are presented in Fig. S8 in the ESM. The

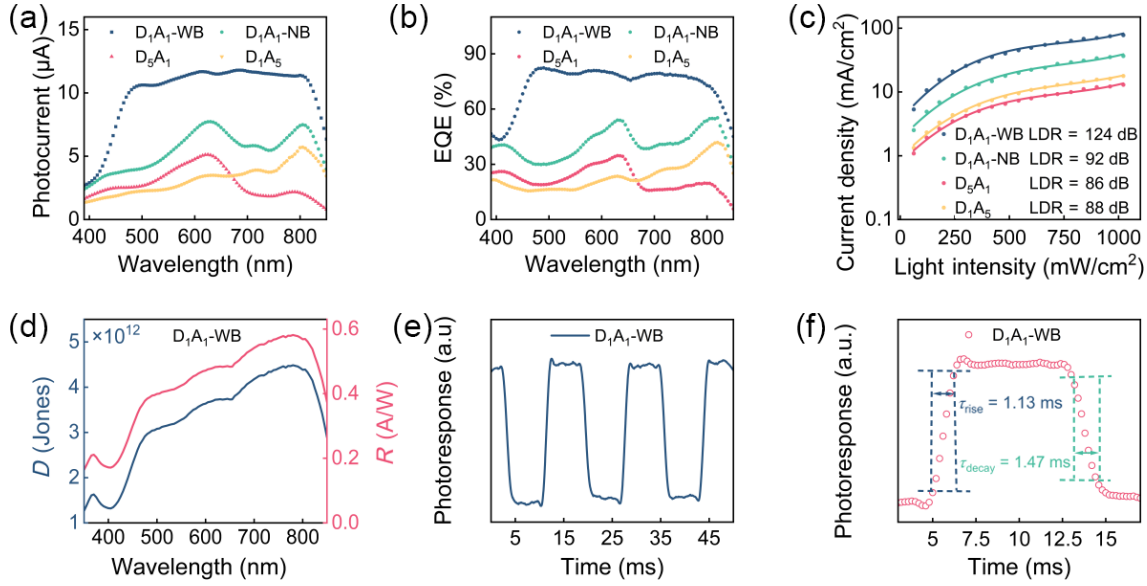

Figure 2 (a) Spectral response and (b) EQE spectra of the OPDs at zero voltage. (c) Photocurrent density of OPDs under different light power illumination at 532 nm illumination. (d) R and D of the OPDs at zero voltage. (e) Time-resolved photoresponse of the D_1A_1-WB photodetector at 532 nm illumination. (f) The rise time and decay time under 532 nm illumination.

light-induced on/off switching was repeatable for multiple cycles. Figure 2(f) shows one cycle of the temporal response, and the rise and decay time were calculated to be 1.13 and 1.47 ms, respectively. All wavelength sensors exhibit millisecond-level response times (Fig. S8 in the ESM), consistent with typical OPDs performance [36, 37].

A schematic diagram of data collection using the wavelength sensor is shown in Fig. 3(a), and Fig. 3(b) outlines the data-acquisition workflow. To quantify broadband monochromatic light, we trained a random forest regressor (RFR) on the spectral fingerprints of four co-processed organic photodetectors. The wavelength recognition logic of this decision tree relies on the hierarchical division of the calibration mechanism and the collaborative driving of multi-device responses (see the ESM). Ultimately, each leaf node stores the average wavelength of samples in the corresponding region, enabling a hierarchical decision-making process (Fig. 3(b)). Similar to the calibration error problem in spectrometers, the device combination of D_1A_1-WB, D_5A_1, and D_1A_5 makes the system highly vulnerable to optical calibration errors and often leads to inaccurate estimation of absolute wavelengths, requiring frequent calibration procedures [38]. As shown in Figs. 2(a) and 2(b), the spectral response of D_1A_1-NB device closely tracks that of D_5A_1 in the short-wavelength region and that of D_1A_5 in the long-wavelength region, which is in good agreement with the correlation analysis (Fig. 3(c)). To address this issue and strengthen the sensor's robustness, we employed D_1A_1-NB to evaluate D_5A_1 against D_1A_1-NB for 400–670 nm and D_1A_5 against D_1A_1-NB for 670–850 nm by exploiting the overlapping spectral windows. This two-point calibration, combined with the broad coverage of D_1A_1-WB, allows a 2 × 2 sensor array to deliver both high wavelength-discrimination accuracy and algorithmic stability (see the ESM).

The feature importance analysis via mean decrease in impurity (MDI) revealed critical sensor contributions (Fig. 3(d)) [39]. The

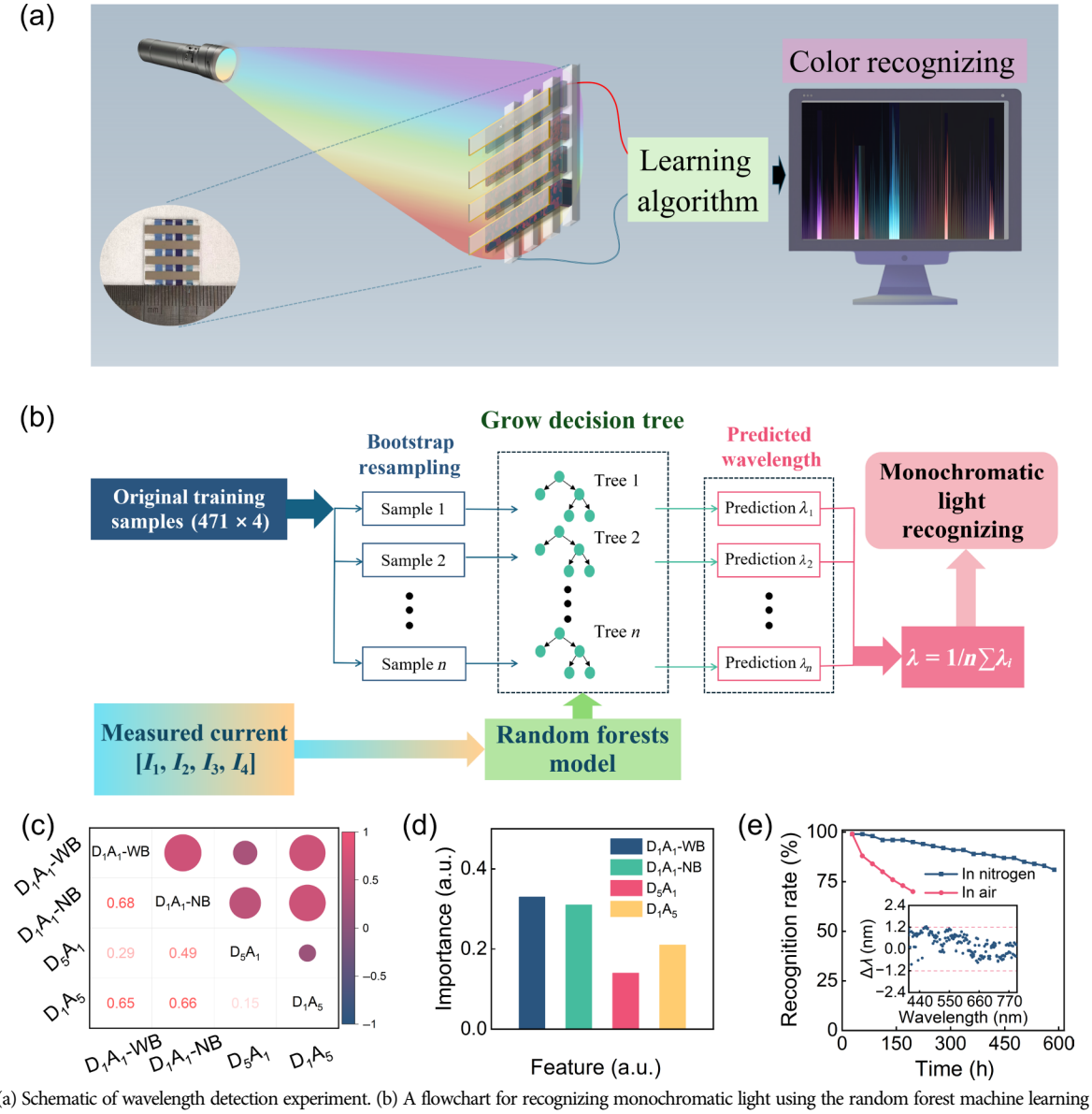

Figure 3 (a) Schematic of wavelength detection experiment. (b) A flowchart for recognizing monochromatic light using the random forest machine learning algorithm. (c) Correlation analysis of D_1A_1-WB, D_1A_1-NB, D_5A_1, and D_1A_5. (d) The importance of various chemical composition in photoactive layer and their contribution to the wavelength determination. (e) The changes in recognition rate when the wavelength sensor is stored separately in nitrogen and ambient environments for a certain period of time. Inset shows errors of calculated wavelengths against actual wavelengths.

normalized photocurrent responses of devices D_1A_1-WB and D_1A_1-NB dominated the predictive power (with a cumulative importance of 64%), and their peak sensitivities showed a strong correlation with the absorption edge characteristics of the active materials. By constructing an ensemble of 200 decision trees with depth regularization to optimize the bias-variance tradeoff, the model achieved a test-set mean absolute error (MAE) of 1.2 nm (Fig. 3(e)). To further evaluate the performance of the optimized integrated self-driven broadband OPDs, their stability was tracked under illumination using a maximum power point tracking method [40]. As shown in Figs. S9–S12 in the ESM, the photocurrent–time and EQE–time curves of the OPDs under nitrogen atmosphere exhibit overall stability with only minor fluctuations, indicating good device stability. After 550 h of storage in a nitrogen-filled glove box, the devices retained 81% of their initial recognition rate. Even after 170 h of storage in air, they still retained 70% of the initial recognition rate (Fig. 3(e)).

To explore the feasibility of panchromatic imaging applications, a scanning imaging system and a working flow chart were developed, as shown in Fig. 4. In imaging applications, the colors obtained by superimposing the three-color channels, i.e., red (R), green (G), and blue (B), on each other include almost all the colors that can be perceived via human vision [41, 42]. As shown in Fig. 4(a), the parameter values (A, B, ..., L) are extracted at the peak wavelength intersections of R (627 nm), G (528 nm), and B (472 nm) to delineate the wavelength sensor's spectral response. When incident light contains multiple color components (R, G, and B), a parametric method is employed to determine the R, G, and B light respective intensities [43]:

$$\begin{bmatrix} \varphi_1 \\ \varphi_2 \\ \varphi_3 \end{bmatrix} = \begin{bmatrix} A & E & I \\ B & F & J \\ C & G & K \\ D & H & L \end{bmatrix}^{-1} \begin{bmatrix} I_1 \\ I_2 \\ I_3 \\ I_4 \end{bmatrix} \quad (2)$$

where φ_1, φ_2, and φ_3 denote the intensities corresponding to B, G, and R light wavelengths, respectively, and I_1, I_2, I_3, and I_4 represent the photocurrents measured from D_1A_1-WB, D_1A_1-NB, D_5A_1, and D_1A_5 at the corresponding wavelength of light under self-driven conditions. Therefore, the color information of incident light can be derived from the calculated light intensities using the color summation method (see the ESM). Furthermore, as

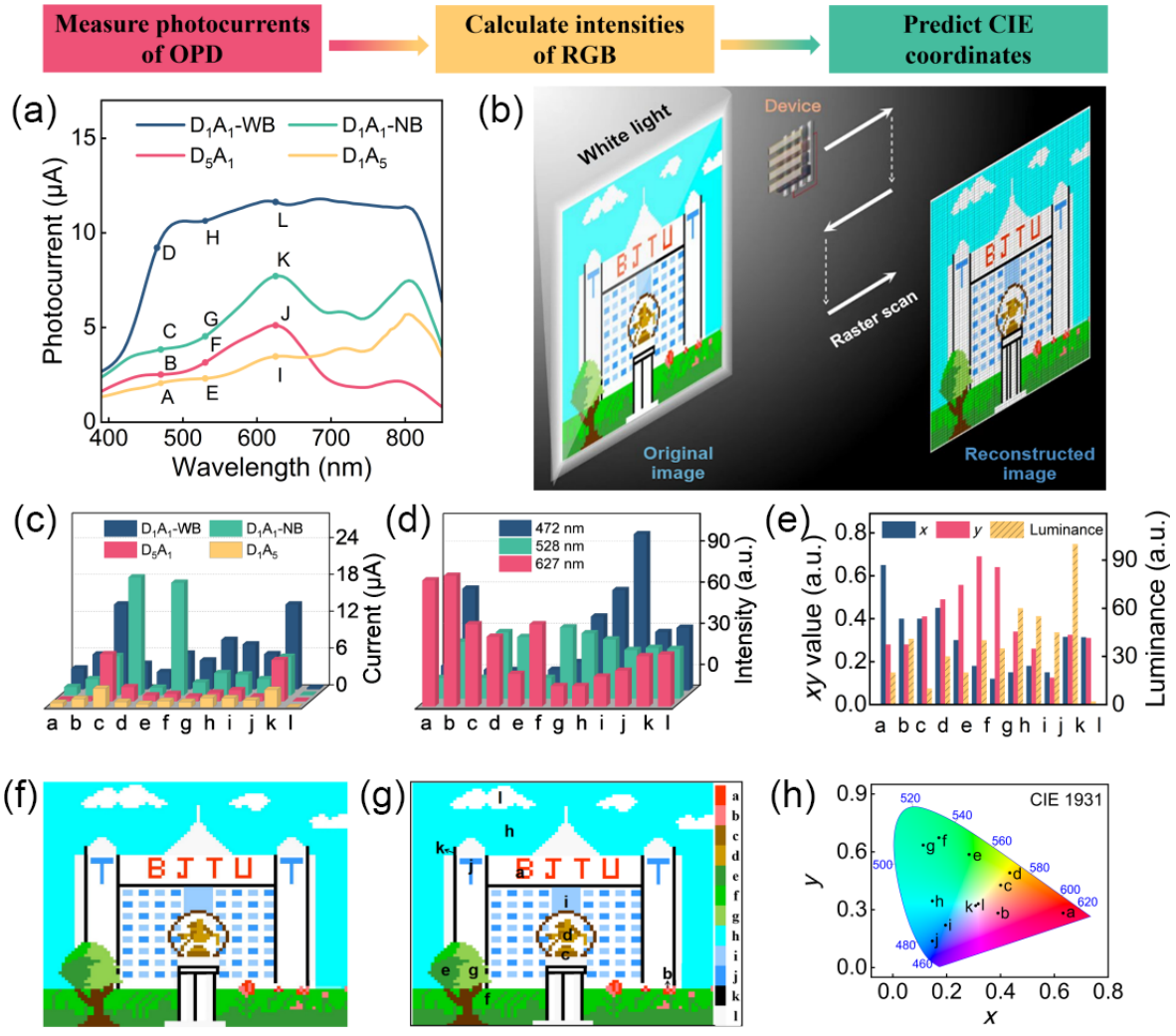

Figure 4 (a) Calculated parameters points for wavelength determination (A–L) and the corresponding spectral response of each device. (b) Schematic illustration of the color imaging setup using wavelength sensor. (c) Photocurrents of I_1, I_2, I_3, and I_4 in regions a–l. (d) The calculated intensities of 472, 528, and 627 nm based on the four photocurrents. (e) The predicted CIE coordinates. (f) Original color pattern that printed onto polymer transparencies. (g) Color image reconstructed using the wavelength sensor. (h) Twelve chromaticity coordinates of the reproduced color image on the 1931 CIE diagram.

shown in Fig. 4(b), a cartoon image consisting of 128 × 128 pixel dots was used to reveal the capability of the wavelength sensor for color imaging applications, where four original photocurrent matrices $[I_x]_{128\times128}$ (x = 1, 2, 3, and 4) can be obtained. The effective illumination area of the wavelength sensors determines the final resolution of the image [15]. Figure 4(c) presents representative values acquired from regions a–l within the original photocurrent matrix $[I_x]_{128\times128}$. As illustrated in Fig. 4(d), the light intensities at the three monochromatic wavelengths, 472, 528, and 627 nm, were determined using Eq. (2). Furthermore, the chromaticity coordinates (x, y) and luminance of the combined light are computed using the color-summation method (see the ESM). Figure 4(e) displays the chromaticity coordinates of the combined light, derived from the data in Fig. 4(d), together with the calibrated luminance values (as shown in the right-hand axis). Together, the chromaticity coordinates and luminance collectively describe the information on mixed light color, enabling accurate display or recognition. Ultimately, the cartoon image is rendered using the image processing function of Python. Using this method, the cartoon image in Fig. 4(f) can be reproduced and displayed in Fig. 4(g), where most colors are reproduced with satisfying similarity. The chromaticity coordinates of regions a–l are shown in the 1931 International Commission on Illumination (CIE) chromaticity diagram (Fig. 4(h)). These findings indicate that as-developed simple-structured wavelength sensors based on PM6:L8-BO hold promise for full-color imaging applications. Table 1 summarizes the performance of the wavelength Sensors and compares them with previously reported studies [15, 44–46, 8, 47, 48], highlighting its superior applicability in full-color imaging recognition.

4 Conclusions

In summary, we successfully developed a series of self-driven broadband OPDs by precisely tuning the donor–acceptor ratio and active layer thickness. The resulting devices deliver distinct spectral responses over a broad range (380–850 nm) with a high-resolution of 1.2 nm. Leveraging device-specific response profiles in combination with machine learning algorithms, the system enables accurate color image recognition, highlighting its potential for computational wavelength analysis and precise color discrimination. The synergy of high wavelength-discrimination accuracy and imaging capability positions these OPDs as strong candidates for advanced machine vision, multispectral imaging, and real-time color detection. Future work will focus on enhancing spectral recognition accuracy via spectral reconstruction techniques and exploring their potential in emerging fields such as biomedical imaging, environmental monitoring, and industrial automation.

Electronic Supplementary Material: Supplementary material (additional experimental details, optical simulation methods, imaging system/algorithm, and Figs. S1–S15) is available in the online version of this article at https://doi.org/10.26599/NR.2026.94908382.

Data availability

All data needed to support the conclusions in the paper are presented in the manuscript and the Electronic Supplementary Material. Additional data related to this paper may be requested from the corresponding author upon request.

Acknowledgements

The authors acknowledge the funding supported by Beijing Natural Science Foundation (Grant No. 1262035), the Talent Fund of Beijing Jiaotong University (No. 2025XKRC004), the National Natural Science Foundation of China (Nos. 62104016 and 62374014), the Natural Science Foundation of Guangdong Province (No. 2023A1515030014), and Shenzhen Fundamental Research Projects (Nos. JCYJ20220531103411026 and ZDSYS201707271014468).

Declaration of competing interest

All the contributing authors report no conflict of interests in this work.

Author contribution statement

Y. J. X.: Conceptualization, methodology, investigation, data curation, formal analysis, visualization, writing – original draft. X. X. Z.: Methodology, investigation, formal analysis, writing – review & editing. J. P. L.: Investigation, data curation. H. M. Y.: Investigation, data curation. K. W.: Investigation. Z. M. H.:

Table 1 Table comparing the performance of wavelength sensor with different material

Principle	Detectivity	Rise/decay time	Wavelength accuracy	Spectral range	Image recognition	Regulatory method	Reference
Perovskite single crystal	10^{12} Jones	—	1.5 nm	265–860 nm	Full-color imaging	Bias voltage	[15]
Broadband multispectral filter array (BMSFA) + chip	—		2.65 nm	400–1000 nm	Real-time imaging	Bias voltage	[44]
MoS_2 optoelectronic synapse	—	54/1362 ms	—	650, 535, and 450 nm	Imaging	Bias voltage	[45]
$CsPbBr_3$ QDs	10^{11} Jones	56/— ms	—	365–525 nm	Color imaging	Bias voltage	[8]
Perovskite crystals	10^{12} Jones		3 nm	400–700 nm	Full-color imaging	Bias voltage	[46]
Graphdiyne (GDY)/2DMs heterostructures	10^{9} Jones	25/10 s	—	405–980 nm	Color imaging	Bias voltage	[47]
Semiconductor/vdW ferroelectric heterojunction	—	29.9/301.7 ms	—	405–635 nm	Color imaging	Bias voltage	[48]
Organic heterojunction	10^{12} Jones	1.13/1.47 ms	1.2 nm	380–850 nm	Full-color imaging	Self-driven	This work

Investigation. Y. K. L.: Investigation. Y. C. X.: Investigation. H. N. L.: Investigation. Z. C.: Visualization, formal analysis. H. L. H.: Resources. H. Z. Z.: Supervision, funding acquisition, writing – review & editing. X. X. Z.: Supervision, writing – review & editing. Y. M. S.: Conceptualization, supervision, project administration, funding acquisition, writing – review & editing. A. W. T.: Conceptualization, supervision, project administration, funding acquisition, writing – review & editing. All authors have read and approved the final manuscript.

Use of AI statement

None.

References

[1] Li, C. Y.; Xiao, Y. T.; Fu, C.; Liang, F. X.; Chen, L. M.; Wu, D.; Luo, L. B. High-accuracy and broadband wavelength sensor with detection region ranging from deep ultraviolet to near infrared light. *Adv. Opt. Mater.* **2022**, *10*, 2101735.

[2] Yi, L. Y.; Tan, H. Q.; Hou, B.; Liu, X. G. X-ray-to-NIR multi-wavelength imaging through stochastic photoluminescence and compressed encoding. *Matter* **2024**, *7*, 2431–2447.

[3] Pan, W.; Wang, L.; Tang, J. S.; Huang, H. Y.; Hao, Z. B.; Sun, C. Z.; Xiong, B.; Wang, J.; Han, Y. J.; Li, H. T. et al. Optoelectronic array of photodiodes integrated with RRAMs for energy-efficient in-sensor computing. *Light: Sci. Appl.* **2025**, *14*, 48.

[4] Guo, J. J.; Tuo, J.; Sun, J. T.; Li, Z. Z.; Guo, X. Y.; Chen, Y. Y.; Cai, R.; Zhong, J.; Xu, L. J. Stretchable multimodal photonic sensor for wearable multiparameter health monitoring. *Adv. Mater.* **2025**, *37*, 2412322.

[5] Hua, X.; Wang, Y. J.; Wang, S. M.; Zou, X. J.; Zhou, Y.; Li, L.; Yan, F.; Cao, X.; Xiao, S. M.; Tsai, D. P. et al. Ultra-compact snapshot spectral light-field imaging. *Nat. Commun.* **2022**, *13*, 2732.

[6] Li, N. X.; Okmi, A.; Jabegu, T.; Zheng, H. K.; Chen, K. C.; Lomashvili, A.; Williams, W.; Maraba, D.; Kravchenko, I.; Xiao, K. et al. van der Waals semiconductor empowered vertical color sensor. *ACS Nano* **2022**, *16*, 8619–8629.

[7] Zhao, T.; Xia, K.; Natali, D.; Pecunia, V. Solution-based integration of vertically stacked organic photodetectors toward easy-to-fabricate filterless multi-color light sensors. *Adv. Opt. Mater.* **2022**, *10*, 2200862.

[8] Wang, W. C.; Tian, W.; Chen, F.; Wang, J. Y.; Zhai, W.; Li, L. Filterless color-selective photodetector derived from integration of parallel perovskite photoelectric response units. *Adv. Mater.* **2024**, *36*, 2404968.

[9] Zhang, T. Y.; Winkler, L. C.; Wolansky, J.; Schröder, J.; Leo, K.; Benduhn, J. High-performance filterless blue narrowband organic photodetectors. *Adv. Funct. Mater.* **2024**, *34*, 2308719.

[10] Bao, J.; Bawendi, M. G. A colloidal quantum dot spectrometer. *Nature* **2015**, *523*, 67–70.

[11] Vasconcelos, T. L.; Vladimirov, S. N.; Pucher, T.; Puebla, S.; Munuera, C.; Hernández, E. R.; Castellanos-Gomez, A. Strain-engineered adaptive 2D photodetectors: A new approach to miniaturized reconstructive spectrometry. *Nano Lett.* **2025**, *25*, 11333–11339.

[12] Fu, Y.; Yuan, M.; Zhao, Y. J.; Dong, M. Q.; Guo, Y. W.; Wang, K.; Jin, C. Q.; Feng, J. G.; Wu, Y. C.; Jiang, L. Gradient bandgap-tunable perovskite microwire arrays toward flexible color-cognitive devices. *Adv. Funct. Mater.* **2023**, *33*, 2214094.

[13] Guo, D. L.; Fu, Q.; Zhang, G. T.; Cui, Y. Y.; Liu, K. Y.; Zhang, X. L.; Yu, Y. L.; Zhao, W. W.; Zheng, T.; Long, H. R. et al. Composition modulation-mediated band alignment engineering from type I to type III in 2D vdW heterostructures. *Adv. Mater.* **2024**, *36*, 2400060.

[14] Liang, F. X.; Fan, R. Y.; Li, J. Y.; Fu, C.; Jiang, J. J.; Fang, T.; Wu, D.; Luo, L. B. Highly sensitive ultraviolet and visible wavelength sensor composed of two identical perovskite nanofilm photodetectors. *Small* **2021**, *17*, 2102987.

[15] Fu, C.; Li, Z. Y.; Wang, J.; Zhang, X.; Liang, F. X.; Lin, D. H.; Shi, X. F.; Fang, Q. L.; Luo, L. B. A simple-structured perovskite wavelength sensor for full-color imaging application. *Nano Lett.* **2023**, *23*, 533–540.

[16] Savage, N. Spectrometers. *Nat. Photon.* **2009**, *3*, 601–602.

[17] Grotevent, M. J.; Yakunin, S.; Bachmann, D.; Romero, C.; Vázquez de Aldana, J. R.; Madi, M.; Calame, M.; Kovalenko, M. V.; Shorubalko, I. Integrated photodetectors for compact Fourier-transform waveguide spectrometers. *Nat. Photon.* **2023**, *17*, 59–64.

[18] Wu, P.; Zhang, T. Y.; Zhu, J. D.; Palacios, T.; Kong, J. 2D materials for logic device scaling. *Nat. Mater.* **2024**, *23*, 23–25.

[19] Yoon, H. H.; Fernandez, H. A.; Nigmatulin, F.; Cai, W. W.; Yang, Z. Y.; Cui, H. X.; Ahmed, F.; Cui, X. Q.; Uddin, M. G.; Minot, E. D. et al. Miniaturized spectrometers with a tunable van der Waals junction. *Science* **2022**, *378*, 296–299.

[20] Deng, W. J.; Zheng, Z. L.; Li, J. Z.; Zhou, R. K.; Chen, X. Q.; Zhang, D. H.; Lu, Y.; Wang, C. W.; You, C. Y.; Li, S. Y. et al. Electrically tunable two-dimensional heterojunctions for miniaturized near-infrared spectrometers. *Nat. Commun.* **2022**, *13*, 4627.

[21] Xue, J. J.; Wang, X.; Xu, G. Y.; Tao, X. Y.; Pan, T. D.; Chen, Z. Y.; Cai, Q.; Shao, P. F.; Yang, G. F.; Huang, Z. L. et al. Multiple exciton generation boosting over 100% quantum efficiency photoelectrochemical photodetection. *Nat. Commun.* **2025**, *16*, 5275.

[22] Sun, L. L.; Wang, J. C.; Matsui, H.; Lee, S.; Wang, W. Q.; Guo, S. Y.; Chen, H. T.; Fang, K.; Ito, Y.; Inoue, D. et al. All-solution-processed ultraflexible wearable sensor enabled with universal trilayer structure for organic optoelectronic devices. *Sci. Adv.* **2024**, *10*, eadk9460.

[23] Li, J. Z.; Wang, J.; Ma, J. Q.; Shen, H. Z.; Li, L.; Duan, X. F.; Li, D. H. Self-trapped state enabled filterless narrowband photodetections in 2D layered perovskite single crystals. *Nat. Commun.* **2019**, *10*, 806.

[24] He, X.; Li, Y. Z.; Yu, H.; Zhou, G. D.; Ke, L. Y.; Yip, H. L.; Zhao, N. A microsized optical spectrometer based on an organic photodetector with an electrically tunable spectral response. *Nat. Electron.* **2024**, *7*, 694–704.

[25] Furlan, F.; Gasparini, N. Organic photovoltaics surpass the 20% efficiency milestone. *Nat. Mater.* **2025**, *24*, 336–337.

[26] Wen, L.; Mao, H. D.; Ban, M. F.; Tan, L. C.; Zhang, J. Y.; Qin, Z.; Zhang, L. F.; Chen, Y. W. Constructing controlled vertical gradient morphology in pseudo-planar heterojunction organic photovoltaics via self-assembled interface orthogonal strategy. *Adv. Mater.* **2025**, *37*, 2503813.

[27] Ahmad, N.; Yuan, J.; Zou, Y. P. One more step towards better stability of non-fullerene organic solar cells: Advances, challenges, future perspectives, and the Era of artificial intelligence. *Energy Environ. Sci.* **2025**, *18*, 5093–5158.

[28] Zhang, J. J.; Duan, X. P.; Li, X. M.; Dai, G. K.; Deng, J. W.; Wang, X. C.; Qiao, J. W.; Wu, H. Z.; Liu, L. M.; Huang, H. D. et al. Achieving 20% efficiency in binary organic solar cells with suppressed non-radiative recombination via triphenylamine halides. *Energy Environ. Sci.* **2025**, *18*, 5378–5388.

[29] Wei, N.; Lu, H.; Wei, Y. Y.; Guo, Y. W.; Song, H. M.; Chen, J. N.; Yang, Z. Y.; Cheng, Y. T.; Bian, Z. Q.; Zhang, W. K. et al. Constructing a dual-fiber network in high efficiency organic solar cells via additive-induced supramolecular interactions with both donor and acceptor. *Energy Environ. Sci.* **2025**, *18*, 2298–2307.

[30] Teixeira, F. L.; Sarris, C.; Zhang, Y.; Na, D. Y.; Berenger, J. P.; Su, Y.; Okoniewski, M.; Chew, W. C.; Backman, V.; Simpson, J. J. Finite-difference time-domain methods. *Nat. Rev. Methods Primers* **2023**, *3*, 75.

[31] Shlager, K. L.; Schneider, J. B. A selective survey of the finite-difference time-domain literature. *IEEE Antennas Propag. Mag.* **1995**, *37*, 39–57.

[32] Feng, W.; Gao, Z. K. Simulation of physical properties of organic photovoltaic cell. *Acta Phys. Sin.* **2008**, *57*, 2567–2573.

[33] Zhang, B.; Chen, W. J.; Chen, H. Y.; Zeng, G.; Zhang, R.; Li, H. X.; Wang, Y. F.; Gu, X. D.; Sun, W. W.; Gu, H. et al. Rapid solidification for green-solvent-processed large-area organic solar modules with > 16% efficiency. *Energy Environ. Sci.* **2024**, *17*, 2935–2944.

[34] Wang, W. B.; Zhang, F. J.; Du, M. D.; Li, L. L.; Zhang, M.; Wang, K.; Wang, Y. S.; Hu, B.; Fang, Y.; Huang, J. S. Highly narrowband photomultiplication type organic photodetectors. *Nano Lett.* **2017**, *17*, 1995–2002.

[35] Einstein, A.; Podolsky, B.; Rosen, N. Can quantum-mechanical description of physical reality be considered complete. *Phys. Rev.* **1935**, *47*, 777–780.

[36] Zhu, Y.; Chen, H. B.; Han, R. M.; Qin, H.; Yao, Z. Y.; Liu, H.; Ma, Y. F.; Wan, X. J.; Li, G. H.; Chen, Y. S. High-speed flexible near-infrared organic photodiode for optical communication. *Nat. Sci. Rev.* **2024**, *11*, nwad311.

[37] Wang, B. H.; Scaccabarozzi, A. D.; Wang, H. Y.; Koizumi, M.; Nugraha, M. I.; Lin, Y. B.; Firdaus, Y.; Wang, Y.; Lee, S.; Yokota, T. et al. Molecular doping of near-infrared organic photodetectors for photoplethysmogram sensors. *J. Mater. Chem. C* **2021**, *9*, 3129–3135.

[38] Lee, D. G.; Song, G.; Lee, C.; Lee, C.; Jang, M. Reconstructive spectrometer using double-layer disordered metasurfaces. *Sci. Adv.* **2025**, *11*, eadv2376.

[39] Li, Z. L.; Pei, S. X.; Chen, Z. Y.; Huang, T. Y.; Wang, X. D.; Shen, L.; Chen, X. B.; Wang, Q. Q.; Wang, D. X.; Ao, Y. F. Machine learning-assisted amidase-catalytic enantioselectivity prediction and rational design of variants for improving enantioselectivity. *Nat. Commun.* **2024**, *15*, 8778.

[40] Zhang, Q. M.; Cheng, Y.; Zhao, S. G.; Zhao, J. W.; Zhao, Z. H.; Tao, L. Optoelectronic reconfigurable 1T-VSe_2/2H-$MoTe_2$ Schottky junction for near-infrared switchable logic. *Commun. Mater.* **2025**, *6*, 119.

[41] Ji, Z.; Liu, Y. J.; Mai, W. Enhancing the photodetection performance of $MAPbI_3$ perovskite photodetectors by a dual functional interfacial layer for color imaging. *Opt. Lett.* **2021**, *46*, 150–153.

[42] Liang, K.; Chow, C. W.; Liu, Y. RGB visible light communication using mobile-phone camera and multi-input multi-output. *Opt. Express* **2016**, *24*, 9383–9388.

[43] Choi, Y. J.; Takahashi, K.; Misawa, N.; Hizawa, T.; Iwata, T.; Sawada, K. Multi-wavelength fluorescence detection of submicromolar concentrations using a filter-free fluorescence sensor. *Sens. Actuat. B: Chem.* **2018**, *256*, 38–47.

[44] Bian, L. H.; Wang, Z.; Zhang, Y. Z.; Li, L. J.; Zhang, Y. N.; Yang, C.; Fang, W.; Zhao, J. J.; Zhu, C. L.; Meng, Q. H. et al. A broadband hyperspectral image sensor with high spatio-temporal resolution. *Nature* **2024**, *635*, 73–81.

[45] Wei, B.; Chen, Y. B.; Han, X. T.; Kang, Y.; Liang, B. J.; Li, C.; Yang, X. K.; Fang, L.; Peng, Y. X. Ultra-low power MoS_2 optoelectronic synapse with wavelength sensitivity for color target recognition. *Sci. China Inf. Sci.* **2025**, *68*, 140406.

[46] Yao, Y. C.; Lee, C. J.; Chen, Y. J.; Feng, J. Z.; Oh, H.; Lue, C. S.; Sheu, J. K.; Lee, Y. J. All-inorganic perovskite quantum-dot optical neuromorphic synapses for near-sensor colored image recognition. *Adv. Sci.* **2025**, *12*, 2409933.

[47] Tang, H. Y.; Shi, W. Q.; Jiang, W. L.; Wang, G. Y.; Tang, M. Y.; Cai, Z. H.; Li, R. T.; Wu, S.; Zhang, G. Q.; Li, J. Wavelength-selective synaptic devices based on Graphdiyne/WSe_2 for multi-color image recognition and neuromorphic computing. *Chem. Eng. J.* **2025**, *517*, 164215.

[48] Bai, J. X.; He, D. W.; Dang, B. J.; Liu, K. Q.; Yang, Z.; Wang, J. R.; Zhang, X. X.; Wang, Y. S.; Tao, Y. Y.; Yang, Y. C. Full van der Waals ambipolar ferroelectric configurable optical hetero-synapses for in-sensor computing. *Adv. Mater.* **2024**, *36*, 2401060.